Journal Name

ARTICLE TYPE

Cite this: DOI: 10.1039/xxxxxxxxxx

High-throughput mechanotransduction in *Drosophila* embryos with mesofluidics†

Ardon Z. Shorr,‡[a] Utku M. Sönmez,‡[b] Jonathan S. Minden,[a] and Philip R. LeDuc[b]

Received Date
Accepted Date

DOI: 10.1039/xxxxxxxxxx

www.rsc.org/journalname

Developing embryos create complexity by expressing genes to coordinate movement which generates mechanical force. An emerging theory is that mechanical force can also serve as an input signal to regulate developmental gene expression. Experimental methods to apply mechanical stimulation to whole embryos have been limited, mainly to aspiration, indentation, or moving a coverslip; these approaches stimulate only a few embryos at a time and require manual alignment. A powerful approach for automation is microfluidic devices, which can precisely manipulate hundreds of samples. However, using microfluidics to apply mechanical stimulation has been limited to small cellular systems, with fewer applications for larger scale whole embryos. We developed a mesofluidic device that applies the precision and automation of microfluidics to the *Drosophila* embryo: high-throughput automatic alignment, immobilization, compression, real-time imaging, and recovery of hundreds of live embryos. We then use *twist*:eGFP embryos to show that the mechanical induction of *twist* depends on the dose and duration of compression. This device allows us to quantify responses to compression, map the distribution of ectopic *twist*, and measure embryo stiffness. For building mesofluidic devices, we describe modifications on ultra-thick photolithography, derive an analytical model that predicts the deflection of sidewalls, and discuss parametric calibration. This "mesomechanics" approach combines the high-throughput automation and precision of microfluidics with the biological relevance of live embryos to examine mechanotransduction. These analytical models facilitate the design of future devices to process multicellular organisms such as larvae, organoids, and mesoscale tissue samples.

1 Introduction

An emerging theory in embryonic development is that gene expression and mechanical forces coordinate development in a reciprocal interplay.[1–3] It is well established that certain developmental genes generate mechanical strain that leads to tissue-specific morphogenetic movement. For example, in *Drosophila*, the transcription factor Twist controls a sequence of events that lead to the apical constriction of ventral cells, changing their shape from columnar to wedge, which collapses the ventral furrow inwards and initiates mesoderm invagination.[4,5] The ventral furrow does not form properly in embryos mutant in *twist*.[6]

Growing evidence suggests that exogenous mechanical forces can be sufficient to directly activate certain genes.[3,7] For example, although *twist* is normally expressed specifically in ventral cells of the *Drosophila* embryo, mechanical compression has been sufficient to trigger ectopic expression of *twist*.[8] The direct mechanical induction of *twist* has been observed by coverslip actuation with piezoelectrics,[8] femtosecond laser pulses,[9] magnetic tweezers,[10] and needle indentation.[11,12] However, the mechanism of mechanotransduction remains unknown. The *Drosophila twist* pathway could be a powerful system to investigate mechanotransduction, but these approaches are labor-intensive, require manual alignment, and process only a few embryos at a time, precluding many biological assays.

One promising approach for manipulating hundreds of embryos simultaneously is microfluidics. Microfluidic approaches have led to semi-automated tools to sort,[13] align,[14,15] immobilize,[16,17] image,[18] and recover processed embryos with minimal intervention. In particular, fabrication using polydimethylsiloxane (PDMS) has many advantages: elasticity and high oxygen-permeability facilitate embryo manipulation; low autofluorescence coupled with transparency in the visible spectrum enable high-resolution fluorescence microscopy. Microfluidic systems have provided spatiotemporal precision for many whole-embryo

[a] *Department of Biological Sciences, Carnegie Mellon University, Pittsburgh, PA.*
[b] *Department of Mechanical Engineering, Carnegie Mellon University, Pittsburgh, PA.*
† Electronic Supplementary Information (ESI) available: [details of any supplementary information available should be included here]. See DOI: 10.1039/b000000x/
‡ These authors contributed equally to this work.

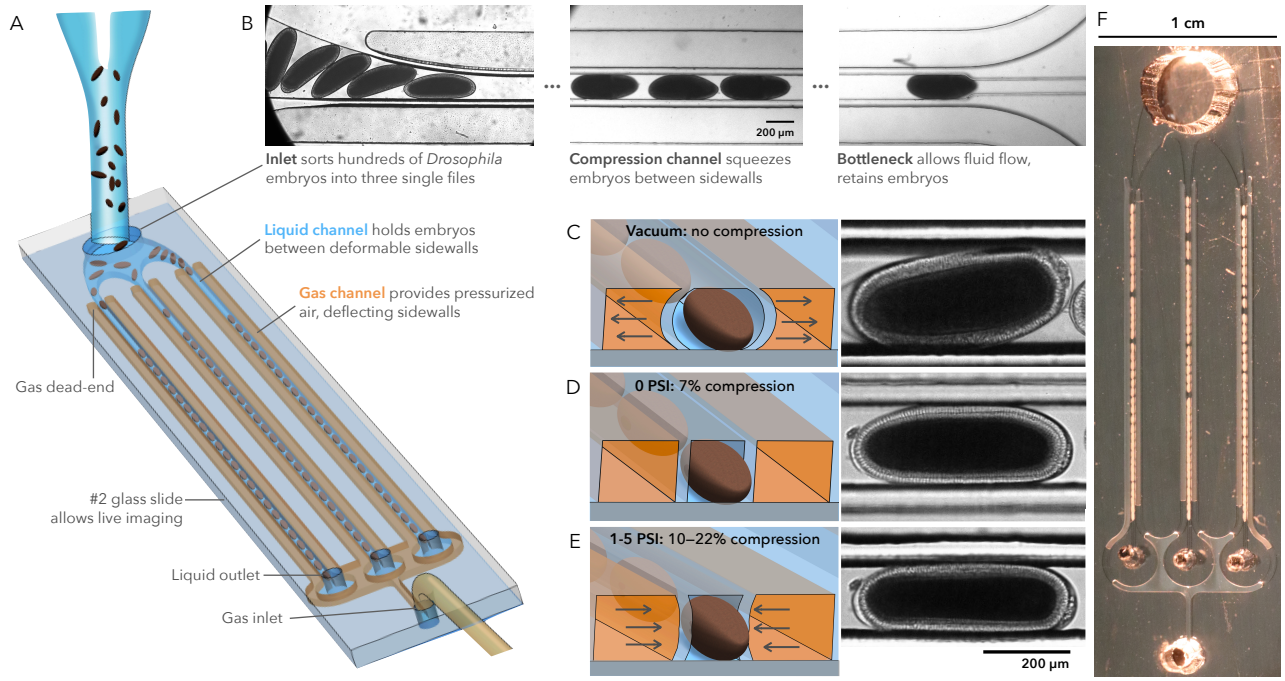

Fig. 1 A mesofluidic device for high-throughput immobilization, imaging, compression, and recovery of *Drosophila* embryos. (A) Illustration of embryos loading into a mesofluidic device. PDMS channels form two interlaced systems: a liquid channel (blue) carries embryos suspended in buffer. A closed gas channel (orange) carries pressurized air. (B) Transmitted light micrographs of embryos in the channel. A narrowing inlet aligns embryos into a single file. The main portion of the channel compresses embryos between two deformable walls. Channels terminate in a bottleneck, allowing fluid flow while retaining embryos. (C–E) Illustrations and micrographs of sidewall deflection. (C) Under vacuum, channel walls expand to load embryos and function as a control condition. (D) At rest, the channel is narrower than the embryo, providing immobilization and compression. (E) Pressurizing the surrounding chamber deflects the channel walls inwards, compressing the embryos further. (F) Photograph of the device with embryos.

interventions, including thermal,[19] chemical,[20,21] acoustic,[22–24] geometric shape,[25,26] and RNAi.[27,28] Microfluidics could be a powerful approach to study mechanotransduction at a high-throughput scale, but mechanical interventions have been limited to smaller cellular systems.[29–32] Microfluidic mechanical interventions that examine multicellular embryos have limited functionality,[33,34] especially in combining immobilization, alignment, and scalability.[17,35]

Here, we describe a mesofluidic device to apply the automation and precision of microfluidics to whole-embryo mechanotransduction (Fig. 1). This device can automatically align, immobilize, and compress hundreds of *Drosophila* embryos. It precisely applies a controlled uniaxial strain using pneumatically actuated flexible sidewalls. This flexibility compensates for the variation in size among embryos, creating a custom width that applies a strain more consistent than conventional techniques. Fabrication on a coverslip allows for live imaging during and after mechanical stimulation, and embryos can be recovered for post-analysis. We describe a method for ultra-thick photolithography, derive an analytical model that predicts sidewall deflection, and discuss parametric calibration to construct future mesofluidic devices. We show this device maintains embryo development, does not induce anoxia, and can apply mechanical stimulation at a high-throughput scale with micrometer accuracy. Using this mesomechanics approach, we map and quantify the dose-dependent and duration-dependent mechanical induction of *twist* during early *Drosophila* development.

2 Methods

2.1 Mesofluidic device fabrication

High aspect-ratio structures remain a fabrication challenge in soft lithography.[36] This challenge is exacerbated for continuous microscale features that cover a mesoscale footprint, such as PDMS sidewalls tens of μm thin, over 200 μm high, and 20,000 μm long. These thin, deep, and trench-like features lead to nonuniform developer exposure across the pattern, and small errors in geometry result in failure of fabrication. We fabricated devices using photolithography and PDMS replica molding[37] with modifications for thick structures (film height $>$ 100 μm) with high aspect ratio (AR $>$ 5) features:

Pouring ultra-thick photoresist. Prior to spin coating, silicon wafers (Si) were cleaned with acetone, isopropyl alcohol (IPA), and deionized water (DI), followed by a dehydration bake at 200 °C for 2 hours. Prior to pouring, ultra-thick photoresist (SU8-2100, MicroChem, MA, USA) was preheated to 60 °C to reduce viscosity to cover the entire wafer. After dehydration bake, the silicon wafer was transferred to a 60 °C hot plate. Preheated photoresist (PR) was poured slowly onto the Si wafer to avoid bubble formation. The PR-coated wafer was left on the hot plate for 5 minutes until the PR evenly coated the entire surface.

Spin coating. Excess PR was removed by a spin coater (WS-400B-6NPP/LITE, Laurell, USA). Pre-spin was at 250 RPM for 30 sec, followed by 400 RPM for 15 sec (acceleration = 85 RPM/sec). PR hanging over the wafer edge was removed with

an acetone-soaked cloth. Spin coating was at 500 RPM for 15 sec (85 RPM/sec) followed by 1,250 RPM for 30 sec (340 RPM/sec).

Acetone dispersion. Surface flaws are common after spin coating a thick layer of highly viscous PR. Surface flaws create uneven contact with the transparency mask during exposure, creating inconsistent features, and small variations in height create large variations in deflection. To homogenize the PR layer, we sprayed acetone on the PR-coated wafer preheated to 50 °C on a leveled hotplate. The sprayed wafer was covered for about 15 minutes until the acetone evaporated. Acetone dispersion lowers the viscosity of PR, removes tiny bubbles and surface divots, increases the uniformity of the PR film, and eliminates the edge bead to provide even contact with the pattern mask. This provides the same benefits of overnight edge bead remover[38] in a few minutes.

Soft bake. The wafer was heated to 95 °C (3 °C/min) on a hot plate and baked for 60 minutes. Then the hotplate was turned off and the wafer slowly cooled down to room temperature.

Exposure. The wafer was exposed to 365 nm ultraviolet light (5 mW/cm^2) for 75 seconds in mask aligner (MA65, Karl-Suss, Germany) through a 20,000 DPI (dots per inch) transparency mask (CAD/Art, CA, USA).

Post-exposure bake. The exposed wafer was heated to 80 °C (3 °C/min) on a hot plate and baked for 20 minutes, followed by a slow cool down for 15 minutes. This longer post-exposure bake at a lower temperature reduces the thermal stress and risk of delamination for thick PR.

Development. The wafer was developed in SU-8 developer (MicroChem, MA, USA) for 20 minutes, then rinsed with fresh developer, IPA, and dried under nitrogen gas. To minimize thermal stress, no further hard bake was applied.

PDMS replica molding. Replica molding followed standard procedures.[39] The patterned wafer was coated with Tridecafluoro-1,1,2,2-tetrahydrooctyl-1-trichlorosilane (TFOCS T2492, United Chemical Technology, PA, USA) for 2 hours in a desiccator. Sylgard 184 PDMS (Dow Corning, Midland, Michigan, USA), was mixed with curing agent at a 10:1 mass ratio and degassed. Degassed PDMS was poured onto the silicon wafer mold and degassed again, then baked in a convection oven at 60 °C for 90 minutes. Cured PDMS was cooled, separated from the mold, and cut to size. Holes were punched for the embryo inlet (4 mm diameter biopsy punch, Integra Miltex, Pennsylvania, PSA), gas inlet (14G blunt needle), and liquid outlets (19G). The patterned surface was cleaned with Scotch tape. The channel was covalently bonded to a 24 x 60 mm #2 glass slide (Warner Instruments, Cincinnati, USA) using oxygen plasma (Harrick Plasma Cleaner, 1 min, 18 W). The assembled device was sandwiched between two thick glass slides separated from the microfluidic system with thin polycarbonate film (McMaster-Carr, Illinois, USA) using a binder clamp to ensure physical contact throughout the PDMS-glass interface during covalent bond development (Fig. S3A). To fine-tune the rigidity of the PDMS sidewalls, the sandwiched device was post-baked in a pre-heated oven at 150 °C (Isotemp Oven, Fischer Scientific, New Hampshire, USA).

2.2 Animals

twist:eGFP flies (w[1118]; Dr[Mio]/TM3, Pw[+mC]=GAL4-twi.G2.3, PUAS-2xEGFPAH2.3, Sb[1] Ser[1]) were a gift from Emily Furbee, University of Pittsburgh. Oregon-R and H2A-RFP; moeGFP/TM6Tb flies were a gift from Brooke McCartney, Carnegie Mellon University. Flies were kept at room temperature in plastic bottles filled with standard *Drosophila* breeding medium. For embryo collection, flies were transferred to 100 mL tri-corner beakers and capped with 60 mm Petri dishes (Fisher Scientific, Pittsburgh, USA) partially filled with a solution containing 1.5% agarose, 2.5% sucrose, 25% apple juice, and 0.15% p-hydroxybenzoic acid methyl ester (methyl paraben to inhibit mold growth) and allowed to gel. A dab of yeast paste (1:2 parts dry yeast to water) was added to each plate. Embryos were collected for three hours, dechorionated for 90 seconds in fresh 50% bleach, washed with distilled water, collected with a cell strainer (Bellco glass), and suspended in egg wash (0.7% NaCl and 0.4% Triton-X 100 in distilled water, 0.2 μm-filtered, light-protected). Embryos were selected under stereoscope to collect those at early cellularization (Stage 5, 2-3 hours after laying)[40] so compression would occur before gastrulation.

2.3 Analytical model for wall deflection

We developed an analytical model to describe the deflection of two sidewalls under pressure (Supplementary Material S1). The deflection of a beam of uniform thickness and loading fixed at both ends is described by the Euler-Bernoulli beam equation:

$$u(x) = \frac{\omega}{24EI}\left(x^4 - 2hx^3 + h^2x^2\right) \tag{1}$$

Where ω is the force per unit length (N/m), E is the Young's modulus (N/m^2), I is the second moment of area (m^4), and h is the height of the sidewall (m). For further definitions and nomenclature, see Supplementary Material S1. If the aspect ratio of the sidewall (h/t) is less than 10, the contribution of shear deformation should also be taken into account. Timoshenko's beam theory[41] includes a secondary term for the contribution of shear deformation:

$$u(x) = \underbrace{\frac{\omega}{24EI}\left(x^4 - 2hx^3 + h^2x^2\right)}_{\text{Pure bending}} + \underbrace{\frac{\omega}{2\kappa GA}(hx - x^2)}_{\text{Contribution of shear}} \tag{2}$$

Where A is the cross-section area of the beam, and κ is Timoshenko's shear coefficient, which is defined for beams with rectangular cross-section as:[42]

$$\kappa = \frac{10(1+\nu)}{12+11\nu} \tag{3}$$

G is the shear modulus, which can be written in terms of Young's modulus and Poisson's ratio (ν) assuming PDMS is fully elastic and isotropic:

$$G = \frac{E}{2(1+\nu)} \tag{4}$$

Relatively wide beams behave more rigidly because they resist lateral deformation from fiber stresses.[43] This stiffening can

be considered with a corrected term for the elastic modulus of the beam, which approaches $E/(1-\nu^2)$ as width approaches infinity.[44] In our system, sidewalls are modeled as vertical beams (Fig. S1), so beam width corresponds to microchannel length L, and the width-to-thickness ratio (L/t) is large. Therefore, the limit value is more accurate for approximating the effective elastic modulus,[44,45] yielding the final equation for deflection:

$$u_{max} = \underbrace{\frac{Ph^4(1-\nu^2)}{32Et^3}}_{\text{Bending}} \cdot \left(1 + \underbrace{\frac{4t^2(12+11\nu)}{5h^2}}_{\text{Shear}}\right) \tag{5}$$

Where P is the pressure applied to the sidewall (N/m^2). This can be expressed in terms of the effective channel width:

$$W' = W - \frac{Ph^4(1-\nu^2)}{16Et^3} \cdot \left(1 + \frac{4t^2(12+11\nu)}{5h^2}\right) \tag{6}$$

Where W is the initial channel width and W' is the effective channel width after applying pressure to deflect two sidewalls.

2.4 Numerical simulation

To predict the shape of the channel wrapping around an embryo, we constructed a 3D CAD model of thin PDMS sidewalls and an embryo in SolidWorks 2016 (Dassault Systèmes, Vélizy-Villacoublay, France), and modeled them in Abaqus (Dassault Systèmes, Vélizy-Villacoublay, France) as fully elastic and isotropic materials with quadratic tetrahedral elements. First, the elastic sidewall deflection was simulated without embryos. Parametric studies determined the Young's modulus of PDMS sidewalls based on experimental results. Then, *Drosophila* embryos were added to the simulation. A similar parametric study used the known Young's modulus of PDMS sidewalls to estimate the Young's modulus of *Drosophila* embryos. Simulations of embryo compression proceeded in two steps. First, embryos received passive compression by a microchannel with a smaller width, which was simulated by displacing the wall towards the fixed embryo. In the second step, embryos received active compression, which was simulated by applying pressure to the deformable PDMS sidewall. Poisson's ratio for PDMS[46] and *Drosophila* was set to 0.4999 to avoid numerical divergence.

2.5 Experimental setup

Pneumatic connections were made with Tygon 3350 Silicone tubing with 1/32" inner diameter (Saint-Gobain, France) and fittings of the appropriate size. Consistent pressure was applied by outfitting a compressed air tank with a custom-made fine Bourdon tube pressure gauge with 0.1 PSI resolution. Consistent vacuum was applied either by running water through a Venturi trap or by using the building vacuum. Embryo wash solution was passed through 0.2 μm syringe filters to avoid clogging the microchannels. As a control for manipulation in the chamber, embryos were mounted on a coverslip glass fixed to the bottom of a plastic Petri dish. Embryos were adhered to the coverslip with a thin layer of glue prepared by dissolving the adhesive from double-sided Scotch tape in heptane. Adhered embryos were covered with a drop of halocarbon oil (series 700; Halocarbon Products, Hackensack, NJ). To apply 50% hypoxia (10% oxygen), the dish setup was placed into a stage-top environmental chamber (Live Cell; Pathology Devices, Westminster, MD) connected to an equal-pressure mixture of argon and air using a T-fitting. To apply anoxia, the dish setup was evacuated for 10 minutes, then placed into the environmental chamber connected only to argon.

2.6 Image acquisition and processing

Compressed embryos were imaged inside the mesofluidic device. Images were acquired on a spinning disk confocal microscope (Nikon Eclipse Ti, running Andor iQ 3.5 software and fitted with an iXon X3 camera). 3D-image stacks were acquired with a 10x objective at 10 μm optical sections for a total depth of 200 μm. The liquid inlet of the mesofluidic device was sealed with a coverslip to prevent evaporation during extended imaging. Time-lapse images were acquired in differential interference contrast (DIC) and fluorescence with a 250 mW 488 nm laser with identical settings for power, exposure, and gain. Each time-lapse session comprised multi-position recordings of 60-120 embryos with 3D-image stacks were acquired every hour for 4 hours. The resulting hyperstacks were manually marked with an elliptical region of interest (ROI), and a custom macro recorded mean pixel values for each slice and frame in Fiji.[47]

3 Results & Discussion

3.1 Design and operation of the mesofluidic device

Our mesofluidic device compresses hundreds of *Drosophila* embryos by aligning them between two sidewalls and deflecting those walls with pressure (Fig. 1). The device consists of two interlaced compartments: a liquid compartment introduces and aligns embryos (Fig. 1, S2). A gas compartment uses microchannels with a closed end to create pneumatic actuation on either side of the liquid compartment, which controls the effective width of the liquid channels to load or compress embryos (Fig. 1E). This configuration was parallelized into three compression channels to triple the throughput of the system. When pressurization bends the sidewalls, it also creates a normal force on the roof of the gas channels, which pushes the thin sidewalls away from the glass slide, which can create leaks. To prevent such leaks, each parallel configuration was separated by a 1.5 mm region of PDMS which provides a large surface area of contact with the glass slide, functioning as a buttress (Fig. S2.) The channels were constructed entirely from PDMS, which is optically transparent and oxygen-permeant.[48] The PDMS structure was bonded to a #2 coverglass, enabling high-resolution fluorescence microscopy.

Embryos were loaded into the device by pipetting them into the large inlet of the liquid compartment (Fig. 1A, ESI video). A narrowing atrium aligned embryos into a single file (Fig. 1B). The section with deformable sidewalls was designed with a narrower width than the embryos (Fig. 2B), preventing embryo entry. When vacuum was applied, the PDMS sidewalls deflected outwards (Fig. 1C), increasing the effective width of the channels, allowing embryo entry. Tilting the device caused embryos to sediment into three parallel compression channels (Fig. 1F, ESI

video). Compression channels terminated in a bottleneck 90 μm wide (Fig. 1B), which allowed fluid flow while retaining embryos.

After the embryos were loaded into the compression channel, the vacuum was removed and the sidewalls recoiled, immobilizing the embryos due to PDMS elasticity (Fig. 1D). Compression focuses embryos to the vertical center of the channel where wall resistance is lowest (Eq. 1, Fig. 2E). Higher compression was achieved by applying pressure to the gas compartment, which deformed the sidewalls inwards (Fig. 1E). Therefore, this system operates in two modes: without external pressure (0 PSI), for immobilization and mild passive compression, and with external pressure (1-5 PSI), to apply an active compressive strain. For post-analysis, embryos were recovered by opening the sidewalls under vacuum, tilting the channel, and collecting embryos from the inlet. Each mesofluidic device accommodated up to 120 embryos in a single run: compression channels were 20 mm long, *Drosophila* embryos were ≈ 500 μm long, and the device operated three channels in parallel. For larger sample size, we developed 40 mm channels that can accommodate up to 240 embryos (Fig. S2C).

3.2 Design calibration for *Drosophila* embryo compression

Compression can be precisely regulated by calibrating five parameters: the width and height of the compression channel, the thickness and the rigidity of the deformable sidewalls, and the applied pressure (Fig. 2A). The final design calibrated for *Drosophila* compression had a channel width of 165 μm (Fig. 2B), channel height of 251.8 μm (Fig. 2C, S3B), wall thickness of 50 μm (Fig. 2D, E, S4), and a post-bake of 2.5 hours at 150 °C (Fig. 2F, G, S5). This resulted in a compression that could be tuned between 0–22% (Fig. 2H, Table 1) with a standard deviation less than 2.4% (Fig. S10, Table S4). Omitting the post-bake, the softer channel walls apply $< 1\%$ compression at 0 PSI to immobilize samples for timelapse imaging (Fig. 2G).

Table 1 Summary of embryo strain in the calibrated mesofluidic device

Pressure (PSI):	Vacuum	0	1	2	3	4	5
Embryo strain:	0%	7%	10%	13%	16%	19%	22%

Channel width. We want a compression channel that is narrower than embryo width to immobilize them passively. However, the channel must also be wide enough under vacuum to allow the biggest embryo to enter without clogging the channel. We measured the width of 140 Stage-5 Oregon-R embryos and found a normal distribution with a mean of 179.6 $\pm$ 1 μm (95% confidence interval, $\sigma = 6$ μm, SEM = 0.5 μm, max = 194.7 μm, Fig. 2B). Based on this distribution, a channel width of 165 μm can immobilize $> 99\%$ of embryos passively. When vacuum is applied, the sidewalls deflected outwards to create an effective width of about 205 μm, allowing the widest embryo to enter (Fig. 2B).

Applied pressure. Pressure is limited by the bond strength between the thin PDMS sidewalls and the glass slide. Any point-sized separation across any 20 mm sidewall causes a leak and failure of the entire channel. Although high pressure increases sample compression range, we found that increasing the pressure past 5 PSI led to unreliable function, and therefore used 5 PSI as an upper limit throughout this study.

Channel height. A key challenge in adapting microfluidics to mesomechanics is maximizing height, which has the strongest influence over deflection (Eq. 5). Maximizing height creates a fabrication challenge in photolithography because the maximum aspect ratio is limited due to diffraction,[49] absorption of light,[50] and chemical diffusion of cross-linking agents,[51] which deform the final geometry and increase the risk of photoresist delaminating from the silicon wafer during curing.[52] Height must be at least greater than the largest embryo (195 μm) to prevent clogging, with some additional allowance for vertical expansion during lateral compression. Height must be at least 250 μm to reasonably deflect at 5 PSI, based on theoretical calculations to deform a 50 μm PDMS wall by 15 μm (Fig. 2C). Based on this target height, we used our modifications on ultra-thick photolithography to fabricate SU-8 molds with an average height of 251.8 μm with uniformity $> 95\%$ (Fig. S3B) as measured by Zygo NewView 7200 3D Optical Surface Profiler (Zygo Corporation, Middlefield, Connecticut, USA).

Wall thickness. To maximize deflection under limited pressure, we also want to minimize wall thickness, which has an inverse-cube influence over deflection (Eq. 5). However, reducing wall thickness reduces their surface area contact with the glass slide, which increases the chance of leaking under pressure. To optimize wall thickness, we used finite element analysis to simulate the deflection of PDMS sidewalls of 35, 50, 90, and 130 μm thickness from 0 to 5 PSI, first by themselves and then with an embryo between them (Fig. 2E, S4). Simulation results were compared to analytical predictions from Eq. 5 (Fig. 2D). Although maximal displacement occurred with 35 μm side walls, such thin walls wrap around the embryo (Fig. S3E, S4), which decreased the surface area exposed to media and could increase the risk of hypoxia. Additionally, these high aspect ratio (h/t) sidewalls create significant difficulty in fabrication for a modest gain in displacement. Walls 90 and 130 μm thick are too stiff to provide adequate compression range (Fig. 2E, S4, Table S2) so we chose 50 μm for the thickness of the deformable sidewalls. At 5 PSI, 50 μm walls decrease the effective width of the channel by 57%, creating a 22.4% compressive strain on embryos. Over 0-5 PSI, this provides a large dynamic range of embryo compression (Fig. 2H, Table 1) within a tractable aspect ratio for fabrication.

Sidewall rigidity. Rigid walls deflect less under pressure but compress the embryo to a greater extent of that deflection. Conversely, soft walls deflect more, but are less compressive, as they wrap around the embryo (Fig. S4). To optimize rigidity, we added a bake step for 0, 2.5, 6, or 15 hours at 150 °C after plasma bonding to increase the rigidity (Young's modulus) of crosslinked PDMS[53] (Fig. S3, S5). These differentially baked channels were simulated numerically (Fig. S5) and measured experimentally (Fig. 2F, G). As expected, longer baking time resulted in walls with an increased Young's modulus (Fig. S3C) that deflected less under pressure (Fig. 2F). To quantify sidewall wrapping, we calculated the ratio of embryo deflection to wall deflection which

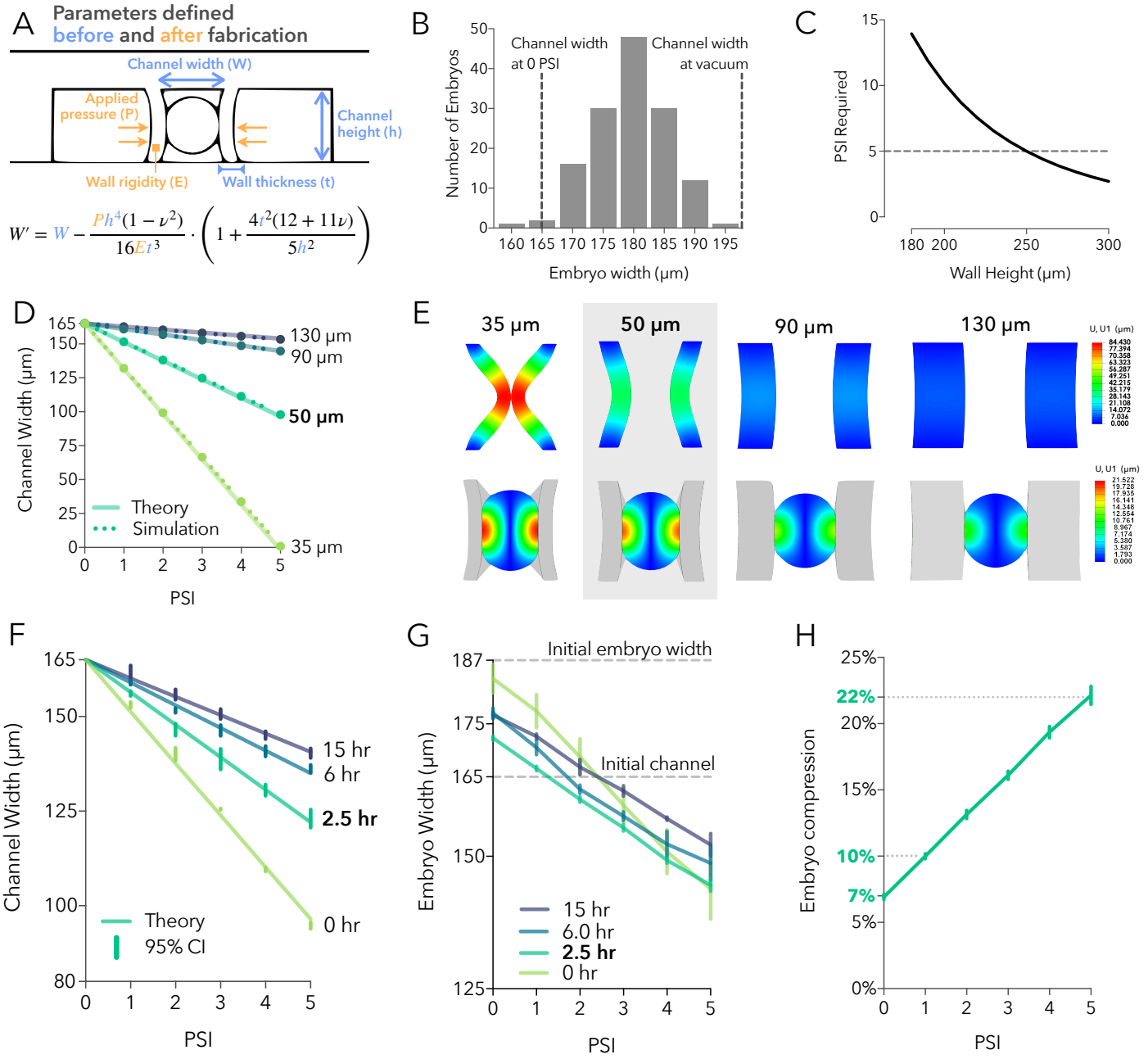

Fig. 2 Defining five parameters for a mesofluidic device: **(A) Overview:** The effective width of a channel under pressure (W') is described by Eq. 6 with five parameters. Three were defined before fabrication (blue) and two were determined afterwards (orange). The goal was to maximize compression while limiting pressure to 5 PSI for reliable function. **(B) Initial channel width** was determined by measuring the width distribution of stage-5 Oregon R embryos (n=140). A channel width of 165 μm immobilizes $> 99\%$ of embryos at rest (0 PSI) while expanding under vacuum to accommodate the widest embryo. **(C) Channel height:** Theoretical prediction of PSI required to sufficiently deflect a wall of varying height. Height was maximized at 250 μm to enable compression at 5 PSI. Wall height has the greatest influence over deflection, as indicated by the polynomial degree of the governing equation. **(D) Wall thickness:** Deflection under pressure was calculated theoretically (solid line) and by numerical simulation (dotted line). Simulation agrees with analytical equation 6 (Table S2). **(E)** Simulated deflection of sidewalls at 5 PSI in a range of thickness with and without embryos (side view cross-section). 50 μm walls (shaded) were selected for the greatest range of compression with the least wrapping around the embryo. **(F) Wall rigidity:** Longer post-cure baking results in more rigid walls (higher Young's Modulus) that deflect less under pressure. Continuous theoretical results with the discrete experimental measurements from 1 PSI increments (95% CI bars). **(G)** Embryo width between sidewalls with a range of rigidity (95% CI bars). 2.5 hours post-cure bake showed the greatest range of compression with minimal wrapping. **(H) Uniaxial compressive strain** (normalized change in embryo width) in the final channel after design optimization (95% CI bars).

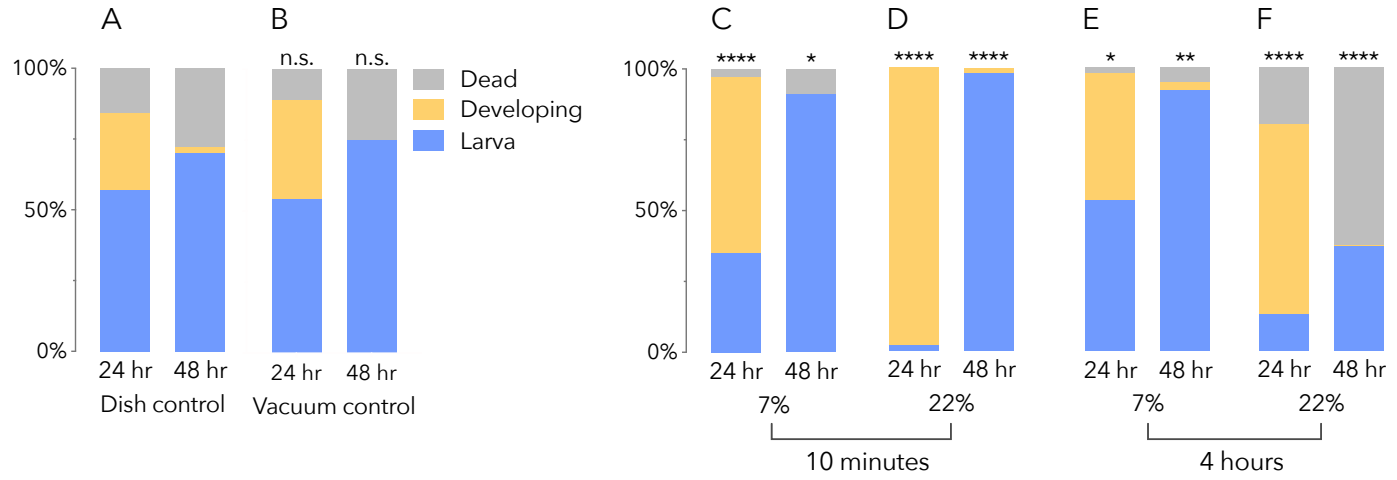

Fig. 3 Survival in the channel. (A) Percentage of wildtype embryos that reached larval stage, were still developing, or dead, 24 and 48 hours after compression (n=111). (B) Vacuum controls (n=68) were loaded into the channel but never compressed. (C, E) Embryos compressed at 7% (n=34, 38) showed greater survival rates than controls. (D) 22% compression for 10 minutes (n=64) led to developmental delays but greater overall survival; (F) 22% compression for 4 hours (n=100) led to death. Statistics compare observed distribution to expected from dish control (Table S1).

we call "compression efficiency" (Fig. S3D). The most rigid walls showed the greatest compression efficiency, but traveled less distance; this resulted in a lower overall compression. The optimal rigidity was the 2.5 hour bake, which showed linear compression up to 22% at 5 PSI with minimal wrapping (Fig. 2H, Table S3).

3.3 Determining Young's modulus of PDMS and *Drosophila*

The Young's modulus of cross-linked PDMS is highly variable, ranging 3 kPa to 3.7 MPa[54] depending on curing agent ratio, curing temperature, duration, size,[55] and age.[56] The analytical model was used to estimate the Young's modulus of PDMS to be 1.88 MPa, comparable to values found by similar fabrication parameters.[53] Based on this value, simulations of embryo compression determined the Young's Modulus of *Drosophila* embryos to be 160 kPa, which is comparable to results from alternative approaches.[57] To determine simulation error, the experimentally observed deflection was used to calculate Young's modulus (Eq. 6) which was then used to run a simulation of deflection. The resulting simulated displacement was compared to the experimentally observed displacement. This process showed the simulation and analytical model to describe deflection within 0.3% error across all sidewall rigidities (Table S3).

Although we model embryo behavior as purely elastic, it is actually viscoelastic,[58] transitioning from viscious to elastic[59] as described by the Kelvin-Voigt model.[60] During this transition, applying a constant force creates a time-dependent strain called viscoelastic creep.[61] To test whether viscoelastic creep affected our setup, we measured the width of compressed embryos over four hours and observed no decrease in embryo width (Fig. S8). This is consistent with reports of other embryonic tissue transitioning to a purely elastic response within several minutes.[60,62] This suggests that viscoelastic creep is not significant in this setup, and the amount of compression applied to embryos can be modeled based on its steady-state elastic response.

3.4 Embryo survival and development

To test whether PDMS channels and compression affect viability, Oregon-R embryos were compressed by 7% or 22% for either 10 minutes (n=34, 64 respectively) or 4 hours (n=38, 100, Fig. 3). As a control for compression, embryos were loaded into the PDMS channel and never compressed; the walls were held open under vacuum ("vacuum control," n=68). As a control for exposure to the device, embryos were cultured in a glass dish (n=111). Embryos were recovered from the device to glass dishes and observed under a brightfield stereoscope at 24 and 48 hours, and scored as first-instar larvae, dead, or developing according to morphological features.[40] Confidence intervals and statistics are in Table S1; two-tailed chi-square test compared observed distribution to expected distribution from dish control.

Vacuum controls showed no developmental difference from dish controls, with 75% reaching larval stage by 48 hours (Fig. 3B vs A) suggesting that exposure to PDMS channels alone does not affect development or survival. Surprisingly, 7% compression for 10 minutes and 4 hours showed greater survival rates compared to dish controls (Fig. 3C, E vs A). One explanation is that the stiff chorion membrane mechanically constrains *Drosophila* embryos, and the standard practice of removing it decreases survival, which is recovered by mild compression! Embryos compressed by 22% for 10 minutes initially showed developmental delay at 24 hours, but ultimately reached first instar by 48 hours at rates greater than dish controls (Fig. 3D vs A). Extending 22% compression to 4 hours reduced survival to 37%; embryos that appeared alive and delayed at 24 hours did not recover by 48 hours (Fig. 3F).

To examine early development in greater detail, we took DIC images of embryos in the channel every hour for 4 hours (Fig. S6). Embryos can be seen at Stage 5 inside the channel (top row). Embryos compressed by 7% appear to proceed through germ-band extension, similar to uncompressed embryos. A minority of embryos compressed by 22% for 4 hours appeared to show no movement for one hour, but then proceeded through germ-band extension (Fig. S6E). These results contradict reports of a ventralized

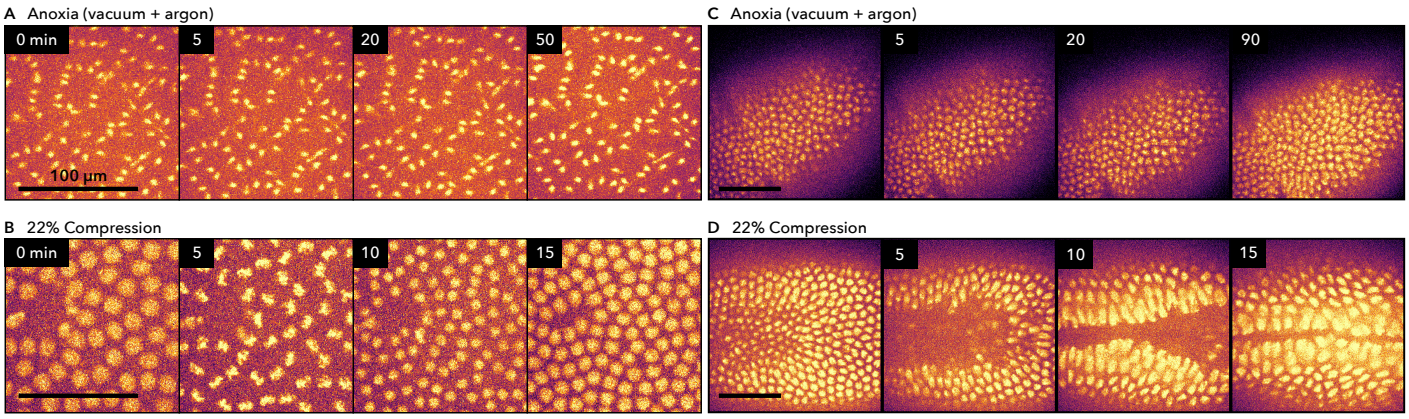

Fig. 4 Channel compression does not induce anoxic arrest. Developmental arrest can be visualized by chromatin condensation, seen in embryos expressing H2A-RFP (color by Matplotlib inferno LUT, all scale bars 100 μm). (A) Embryos kept anoxic by 10 minutes of vacuum followed by continuous argon show morphogenic freezing; nuclei in anaphase stay arrested for over 50 minutes. (B) In contrast, compressed embryos pass through anaphase normally, doubling nuclei over 10 minutes. (C) Anoxic embryos also show chromatin condensation, visible as puncta in nuclei that fail to divide over 90 minutes. (D) In contrast, compressed embryos show diffuse fluorescence indicating decondensed chromatin, and continue development.

phenotype that fails to extend the germ band after compression.[8] This difference in developmental milestones could be from several factors: (1) Previously, embryos were observed up to 50 minutes before concluding the phenotype was stable; observing over 4 hours shows recovery is possible (Fig. S6E); (2) There might be effects from the differences in genetic background in fly stocks used in these experiments; (3) There might be effects that stem from different methods of compression that result in variations in strain magnitude and consistency.

Comparison of compression methods

To compare our compression to previous work, we numerically simulated the approach of Farge 2003.[8] Specifically, Farge's compression was (1) applied vertically and observed indirectly by 10% lateral expansion, orthogonal to the direction of compression; (2) applied by rigid glass. We simulated embryo deformation by a rigid plate sufficient to create a 10% lateral expansion (Fig. S9). The resulting inferred compression was 25–34% (Table S5). This inferred uniaxial compression is larger because shape change begins vertically; height decreases substantially before significant lateral expansion occurs. This greater compression may explain observed differences in developmental arrest.

Based on numerical simulations, compression by glass is more variable than compression by PDMS. When compressing walls are rigid, channel width is strict, resulting in greater compression for wider embryos (Fig. S10A). In contrast, when compressing walls are flexible, wider embryos can resist wall displacement, creating an effective channel width unique to each embryo (Fig. S10B). As a result, compressive strain is more variable under stiffer walls. This variation can be quantified by simulating compression of embryos with mean width (180 μm), maximum width (195 μm), and minimum width (160 μm) in the same channel (Fig. S10). In lateral compression by glass, standard deviation of strain was 39% of the mean (CoV). In lateral compression by PDMS, strain variance was reduced to 11% CoV (Table S4). In vertical compression by glass sufficient to obtain 10% lateral expansion, the uniaxial compressive strain ranges 25%–34%, 16% CoV (Table S5).

Overall, the channel itself neither delays nor destroys *Drosophila* embryos. Compression appears to switch from beneficial to harmful above a threshold of magnitude and time. These observations highlight the importance of long-term analysis, as developmental outcomes can drastically diverge days after mechanostimulation. Flexible PDMS sidewalls apply compression that is more consistent and directly measurable, which helps compare results across multiple studies.

Anoxia

The gas permeability of PDMS is well established for cell culture,[48] but not for whole-organism *Drosophila*. Anoxia produces a rapid developmental arrest during which interphase chromosomes prematurely condense.[63] Chromatin condensation can be visualized by fusing histone H2A to a red fluorescent protein (H2A-RFP). As a positive control, anoxia was induced by placing H2A-RFP embryos in a coverslip dish and evacuating for 10 minutes, then under a continuous flow of argon in a stage-top environmental chamber. As expected, nuclei remained developmentally arrested (Fig. 4A) and chromatin condensation was observed as fluorescent puncta (Fig. 4C). In contrast, embryos in the mesofluidic device proceeded through nuclear division with typical timing (Fig. 4B), showed decondensed chromatin, and large-scale morphogenetic movement (Fig. 4D) even at 5 PSI (22% compression). These results confirm that the mesofluidic device provides sufficient oxygen to prevent anoxia.

3.5 Mechanical induction of *twist*

Mechanical induction of *twist* was first described by Farge in 2003.[8] To examine whether mesofluidic compression also induces *twist* expression, we monitored fluorescence from the *twist* promotor driving eGFP, measured every hour for 4 hours (Fig. 5). In unconstrained embryos, *twist*:eGFP localized to a stripe of ventral furrow cells, indicating normal expression (Fig. 5A). Constrained embryos showed widespread expression that was brighter and ectopic (Fig. 5B–E). This is consistent with the hy-

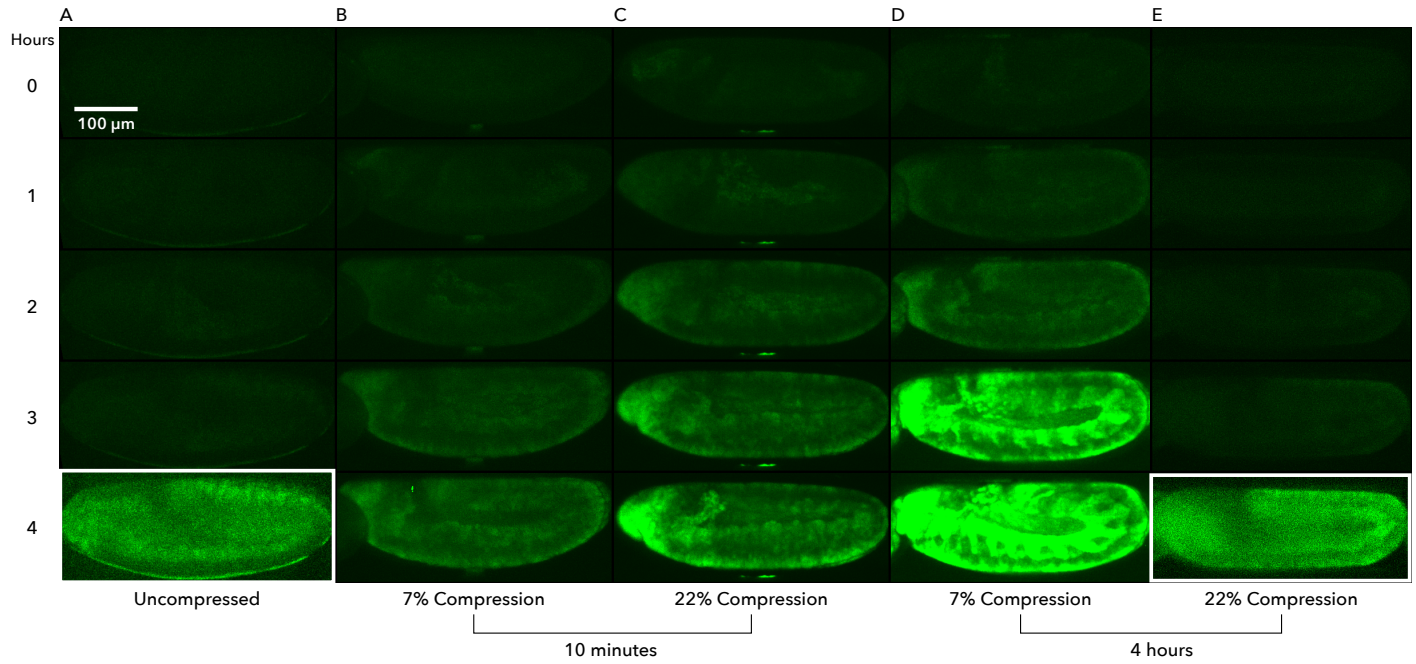

Fig. 5 Ectopic distribution of *twist*:eGFP in compressed embryos. *twist*:eGFP fluorescence was measured every hour over 4 hours. Pixel value settings are the same for all images, except for A4 and E4 (white border) to show patterning. (A) Uncompressed embryos show a ventral stripe of *twist*:eGFP expression. (B, C) Embryos compressed for 10 minutes show an increase in *twist*:eGFP over 4 hours. (D) Embryos compressed by 7% for 4 hours show substantial increase in fluorescence. (E) Embryos compressed by 22% for 4 hours show low but ectopic fluorescence.

pothesis that *twist* expression is coordinated by mechanical force; during normal development, *twist* is selectively expressed in ventral furrow cells that experience internal mechanical forces due to morphogenetic movement. When the entire embryo is compressed, the whole organism experiences mechanical stimulation, which is sufficient to induce ectopic expression of *twist*.

To quantify the increase in *twist*:eGFP fluorescence, we measured mean fluorescence pixel intensity. As a control for compression, embryos were introduced into the chamber with the walls held open by vacuum, and all significance tests were made relative to this vacuum control. As a control for handling embryos in the channel, embryos were observed under halocarbon oil on a coverslip (dish control). Four hours after compression, all embryos showed an increase in *twist*:eGFP fluorescence (Fig. 6A). Embryos compressed for 10 minutes showed a significant dose-dependent increase in *twist*:eGFP when compressed by 7% ($p < 0.01$) and 22% ($p < 0.0001$; ordinary one-way ANOVA to vacuum control, Fig. 6). Embryos also showed a duration-dependent increase in *twist*:eGFP when 7% compression was extended to 4 hours ($p < 0.0001$, Fig. 6B). In the 22% 4-hour condition, *twist*:eGFP fluorescence was not significantly different from vacuum controls in magnitude. Yet the distribution of that expression remained ectopic (Fig. 5 inset, E vs A). This is consistent with the idea that both the dose and the duration of compression are biologically relevant. One explanation for the lower fluorescence magnitude is that embryos in this condition are already committed to die within 48 hours (Fig. 3F), perhaps because this amount of compression disrupts the integrity of the embryo.

Hypoxia

The mesofluidic device provides sufficient oxygen to avoid full anoxia, but also confines embryos to a small volume of media and applies vacuum during loading, which could induce partial hypoxia. Hypoxia is a confounding explanation for the increase in *twist*:eGFP after compression: hypoxia-inducible factor (HIF-1α) may upregulate *twist* mRNA by binding to a hypoxia-responsive element in the proximal promoter.[64,65] This pathway was demonstrated in tumor cell lines and in *C. elegans* mutant for the *twist* homolog (hlh-8), but remains unconfirmed in *Drosophila*.[65]

To investigate whether hypoxia could explain the increase in *twist*:eGFP after compression, we intentionally induced a 50% oxygen shortage by flowing equal pressures of compressed atmospheric air and argon through a stage-top environmental chamber. Embryos continued to develop (Fig. S7), and the resulting *twist*:eGFP fluorescence after 4 hours was reduced compared to normoxia controls ($p < 0.0001$, Fig. 6, S7), likely due to interference with eGFP folding.[66] This suggests that hypoxia cannot explain the increase in *twist*:eGFP after compression.

The increase in fluorescence in vacuum controls compared to dish controls (Fig. 6) was unexpected. One explanation is that in a dish, when sample size is sufficiently large, standard techniques introduce clusters of embryos that compete for oxygen, which inhibits eGFP. The mesofluidic device may provide better access to oxygen than dish controls by maintaining consistent density and surrounding embryos with a thin wall of oxygen-permeant PDMS.

Another explanation is that the increase in fluorescence in vacuum controls is an artifact of handling. While switching tubing for microscopy, the vacuum was discontinuous for approximately

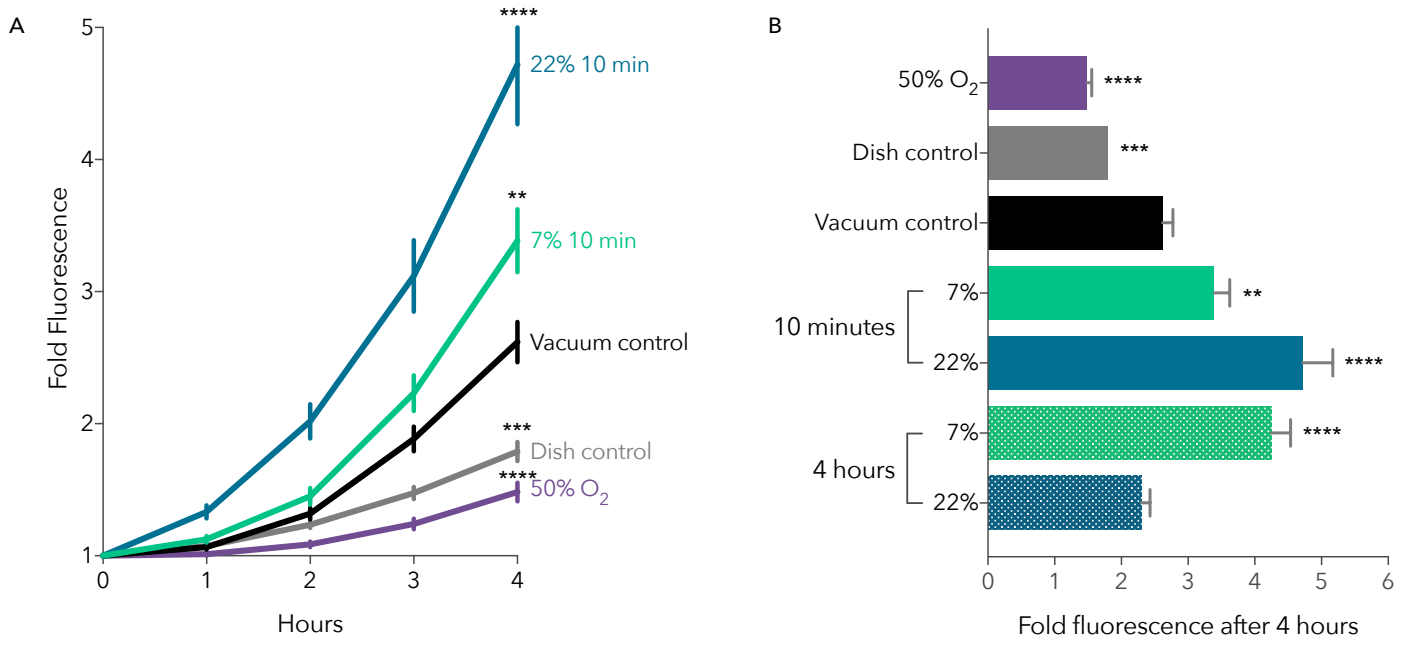

Fig. 6 Mechanical induction of *twist* expression. (A) *twist*:eGFP fluorescence was measured every hour over 4 hours after compression. Embryos show a significant increase in mean fluorescence when compressed for 10 minutes by 7% (0 PSI, $p < 0.01$) and 22% (5 PSI, $p < 0.0001$; Ordinary one-way ANOVA to vacuum control, SEM bars). Vacuum controls were introduced into the channel with the walls held open; dish controls remained outside the channel. Hypoxia (50% O_2) decreased *twist*:eGFP expression ($p < 0.0001$). (B) Summary of *twist*:eGFP fluorescence after 4 hours (SEM bars, ordinary one-way ANOVA to vacuum control).

one minute, causing a brief flexing of the sidewalls, which could trigger an intermediate *twist* response. Consistent with this hypothesis, vacuum controls in survival experiments that did not require switching tubing also did not show an intermediate response between dish control and compression (Fig. 3B vs A). Taken together, the potential for rapid induction of *twist* expression highlights the need for precise temporal control when studying mechanotransduction.

4 Conclusions

We developed a novel mesofluidic device that automatically aligns and immobilizes hundreds of *Drosophila* embryos without external force. This device precisely compresses hundreds of embryos using deformable pressure-actuated sidewalls, allows for live imaging, and retrieval of live embryos for post-analysis. We describe a method for consistent ultra-thick photolithography, derive an analytical model that describes sidewall deflection, and discuss the calibration of five parameters critical to designing mesofluidic devices. The device itself does not affect survival or development and does not induce anoxic arrest. Using this device, we measure the Young's modulus of PDMS sidewalls and *Drosophila* embryos, and observe that compressing embryos is sufficient to trigger the mechanical induction of *twist* that is dose- and duration-dependent.

This approach facilitates the design of future devices for high-throughput mechanotransduction and imaging of larvae, embryos, oocytes, organoids, and small adults such as *Danio rerio* and *C. elegans*. By tuning the rigidity of PDMS, the device can operate without a pressure tank to immobilize samples for timelapse imaging while maintaining access to oxygen. The bottleneck constriction at the end of the compression channel allows for rapid exchange of media around immobilized samples, enabling chemical stimulation and on-chip staining inside the microchannel. This enables combined mechanical and chemical stimulation with real-time imaging. The ability to process many whole-tissue samples and precisely apply mechanical stimulation enables us to explore the induction of *twist*, and to map out novel mechanosensitive pathways in meso-scale organisms.

Conflicts of interest

There are no conflicts to declare.

Acknowledgements

Thanks to Rebecca Taylor, Paul Steif, Fred Lanni, and Rachel Koh for their discussion on the analytical model of wall deflection.

This work was supported in part by the Air Force Office of Scientific Research (FA9550-18-1-0262), Office of Naval Research (N00014-17-1-2566), and Pennsylvania Department of Health (SAP4100077084). UMS was partially supported by Turkish Education Agency (TEV).

Notes and references

1 M. E. Fernández-Sánchez, T. Brunet, J.-C. Röper and E. Farge, *Annual Review of Cell and Developmental Biology*, 2015, **31**, 373–397.

2 E. Brouzés, W. Supatto and E. Farge, *Biology of the Cell*, 2004, **96**, 471–477.

3 E. Brouzés and E. Farge, *Current opinion in genetics & development*, 2004, **14**, 367–374.

4 Y. T. Ip and T. Gridley, *Current opinion in genetics & development*, 2002, **12**, 423–429.

5 M. Costa, E. T. Wilson and E. Wieschaus, *Cell*, 1994, **76**, 1075–1089.

6 D. St Johnston and C. Nüsslein-Volhard, *Cell*, 1992, **68**, 201–219.

7 M. A. Wozniak and C. S. Chen, *Nature Reviews Molecular Cell Biology*, 2009, **10**, 34–43.

8 E. Farge, *Current Biology*, 2003, **13**, 1365–1377.

9 W. Supatto, D. Débarre, B. Moulia, E. Brouzés, J.-L. Martin, E. Farge and E. Beaurepaire, *Proceedings of the National Academy of Sciences of the United States of America*, 2005, **102**, 1047–1052.

10 N. Desprat, W. Supatto, P.-A. Pouille, E. Beaurepaire and E. Farge, *Developmental Cell*, 2008, **15**, 470–477.

11 P.-A. Pouille, P. Ahmadi, A.-C. Brunet and E. Farge, *Science Signaling*, 2009, **2**, ra16.

12 B. A. Filas, G. Xu and L. A. Taber, *Methods in molecular biology (Clifton, N.J.)*, 2015, **1189**, 3–16.

13 C. C. Chen, S. Zappe, O. Sahin, X. J. Zhang, M. Fish, M. Scott and O. Solgaard, *Sensors and Actuators B: Chemical*, 2004, **102**, 59–66.

14 K. Chung, Y. Kim, J. S. Kanodia, E. Gong, S. Y. Shvartsman and H. Lu, *Nature Methods*, 2010, **8**, 171–176.

15 T. J. Levario, M. Zhan, B. Lim, S. Y. Shvartsman and H. Lu, *Nature Protocols*, 2013, **8**, 721–736.

16 R. W. Bernstein, X. Zhang, S. Zappe, M. Fish, M. Scott and O. Solgaard, *Sensors and Actuators A: Physical*, 2004, **114**, 191–196.

17 X. Zhang, C.-C. Chen, R. W. Bernstein, S. Zappe, M. P. Scott and O. Solgaard, *Journal of Microelectromechanical Systems*, 2005, **14**, 1187–1197.

18 X. Cui, L. M. Lee, X. Heng, W. Zhong, P. W. Sternberg, D. Psaltis and C. Yang, *Proceedings of the National Academy of Sciences*, 2008, **105**, 10670–10675.

19 G. T. Dagani, K. Monzo, J. R. Fakhoury, C.-C. Chen, J. C. Sisson and X. Zhang, *Biomedical Microdevices*, 2007, **9**, 681–694.

20 Y. Kim, M. Hazar, D. S. Vijayraghavan, J. Song, T. R. Jackson, S. D. Joshi, W. C. Messner, L. A. Davidson and P. R. LeDuc, *Proceedings of the National Academy of Sciences*, 2014, **111**, 14366–14371.

21 M. Gershow, M. Berck, D. Mathew, L. Luo, E. A. Kane, J. R. Carlson and A. D. T. Samuel, *Nature Methods*, 2012, **9**, 290–296.

22 T. Ohyama, T. Jovanic, G. Denisov, T. C. Dang, D. Hoffmann, R. A. Kerr and M. Zlatic, *PLoS ONE*, 2013, **8**, e71706–21.

23 R. Ghaemi, P. Rezai, B. G. Iyengar and P. R. Selvaganapathy, *Lab on a Chip*, 2015, **15**, 1116–1122.

24 W. Zhang, Z. Yan, L. Y. Jan and Y. N. Jan, *Proceedings of the National Academy of Sciences of the United States of America*, 2013, **110**, 13612–13617.

25 S. R. Lockery, K. J. Lawton, J. C. Doll, S. Faumont, S. M. Coulthard, T. R. Thiele, N. Chronis, K. E. McCormick, M. B. Goodman and B. L. Pruitt, *Journal of neurophysiology*, 2008, **99**, 3136–3143.

26 S. Park, H. Hwang, S.-W. Nam, F. Martinez, R. H. Austin and W. S. Ryu, *PLoS ONE*, 2008, **3**, e2550–5.

27 S. Zappe, M. Fish, M. P. Scott and O. Solgaard, *Lab on a Chip*, 2006, **6**, 1012–8.

28 D. Delubac, C. B. Highley, M. Witzberger-Krajcovic, J. C. Ayoob, E. C. Furbee, J. S. Minden and S. Zappe, *Lab on a Chip*, 2012, **12**, 4911–9.

29 V. Sivagnanam and M. A. M. Gijs, *Chemical Reviews*, 2013, **113**, 3214–3247.

30 F. Kurth, K. Eyer, A. Franco-Obregón and P. S. Dittrich, *Current Opinion in Chemical Biology*, 2012, **16**, 400–408.

31 J. D. Kubicek, S. Brelsford, P. Ahluwalia and P. R. LeDuc, *Langmuir : the ACS journal of surfaces and colloids*, 2004, **20**, 11552–11556.

32 R. L. Steward, C.-M. Cheng, D. L. Wang and P. R. LeDuc, *Cell biochemistry and biophysics*, 2010, **56**, 115–124.

33 J. R. Fakhoury, J. C. Sisson and X. Zhang, *Microfluidics and Nanofluidics*, 2009, **6**, 299–313.

34 D. T. Chiu, A. J. deMello, D. Di Carlo, P. S. Doyle, C. Hansen, R. M. Maceiczyk and R. C. R. Wootton, *CHEMPR*, 2017, **2**, 201–223.

35 C. E. Narciso, N. M. Contento, T. J. Storey, D. J. Hoelzle and J. J. Zartman, *Biophysical Journal*, 2017, **113**, 491–501.

36 A. Folch, *Introduction to bioMEMS*, 2016.

37 Y. N. Xia and G. M. Whitesides, *Annual Review of Materials Science*, 1998, **28**, 153–184.

38 H. Lee, K. Lee, B. Ahn, J. Xu, L. Xu and K. W. Oh, *Journal of Micromechanics and Microengineering*, 2011, **21**, 125006.

39 D. Qin, Y. Xia and G. M. Whitesides, *Nature Protocols*, 2010, **5**, 491–502.

40 J. A. Campos-Ortega and V. Hartenstein, *The embryonic development of Drosophila melanogaster*, 2013.

41 J. Carrer, W. J. Mansur, R. F. Scuciato and S. A. Fleischfresser, *Blucher Mechanical Engineering Proceedings*, 2012.

42 G. R. Cowper, *Journal of Applied Mechanics*, 1966, **33**, 335–340.

43 W. C. Young and R. G. Budynas, *Roark's Formulas for Stress and Strain*, McGraw-Hill, New York, 7th edn, 2006.

44 F. I. Baratta, *Journal of the American Ceramic Society*, 1981, **64**, C86–C86.

45 R. D. Cook and W. C. Young, *Advanced mechanics of materials*, Prentice Hall, Upper Saddle River, NJ, 1999, vol. 2.

46 R. H. Pritchard, P. Lava, D. Debruyne and E. M. Terentjev, *Soft Matter*, 2013, **9**, 6037–6045.

47 J. Schindelin, I. Arganda-Carreras, E. Frise, V. Kaynig, M. Longair, T. Pietzsch, S. Preibisch, C. Rueden, S. Saalfeld, B. Schmid, J.-Y. Tinevez, D. J. White, V. Hartenstein, K. Eliceiri, P. Tomancak and A. Cardona, *Nature Methods*, 2012, **9**, 676–682.

48 E. Berthier, E. W. K. Young and D. Beebe, *Lab on a Chip*, 2012, **12**, 1224–1237.

49 Y. J. Chuang, F. G. Tseng and W. K. Lin, *Microsystem Technologies*, 2002, **8**, 308–313.

50 Z. G. Ling, K. Lian and L. Jian, Microlithography 2000, 2000, pp. 1019–1027.

51 H. Lorenz, M. Despont, P. Vettiger and P. Renaud, *Microsystem Technologies*, 1998, **4**, 143–146.

52 C.-H. Lin, G.-B. Lee, B.-W. Chang and G.-L. Chang, *Journal of Micromechanics and Microengineering*, 2002, **12**, 590–597.

53 I. D. Johnston, D. K. McCluskey, C. K. L. Tan and M. C. Tracey, *Journal of Micromechanics and Microengineering*, 2014, **24**, 035017.

54 Z. Wang, A. A. Volinsky and N. D. Gallant, *Journal of Applied Polymer Science*, 2014, **131**, 41050.

55 M. Liu, J. Sun, Y. Sun, C. Bock and Q. Chen, *Journal of Micromechanics and Microengineering*, 2009, **19**, 035028.

56 V. Placet and P. Delobelle, *Journal of Micromechanics and Microengineering*, 2015, **25**, 035009.

57 Y. Shen, N. Xi and R. Zhang, *ieeexplore.ieee.org*, 31–36.

58 L. Z. Yanez and D. B. Camarillo, *Molecular human reproduction*, 2017, **23**, 235–247.

59 Y. Fung, *Biomechanics: mechanical properties of living tissues*, 2013.

60 G. Forgacs, R. A. Foty, Y. Shafrir and M. S. Steinberg, *Biophysical Journal*, 1998, **74**, 2227–2234.

61 O. Campàs, *Seminars in Cell and Developmental Biology*, 2016, **55**, 119–130.

62 W. A. Malik, S. C. Prasad, K. R. Rajagopal and L. Preziosi, *Mathematics and Mechanics of Solids*, 2007, **13**, 81–91.

63 V. E. Foe and B. M. Alberts, *Journal of Cell Biology*, 1985, **100**, 1623–1636.

64 M.-H. Yang and K.-J. Wu, *Cell Cycle*, 2014, **7**, 2090–2096.

65 M.-H. Yang, M.-Z. Wu, S.-H. Chiou, P.-M. Chen, S.-Y. Chang, C.-J. Liu, S.-C. Teng and K.-J. Wu, *Nature Cell Biology*, 2008, **10**, 295–305.

66 C. Coralli, M. Cemazar, C. Kanthou, G. M. Tozer and G. U. Dachs, *Cancer Research*, 2001, **61**, 4784–4790.